JOURNAL OF MATERIALS SCIENCE **39** (2004) 215–224

Characteristics of α-dendritic and eutectic structures in Sr-treated Al—Si casting alloys

L. LIU, A. M. SAMUEL, F. H. SAMUEL
Département des Sciences appliquées, Université du Québec à Chicoutimi, Chicoutimi (Québec), Canada G7H 2B1
E-mail: fhsamuel@uqac.ca

H. W. DOTY
Materials Engineering, GM Powertrain Group, Metal Casting Technology, Inc., Milford, NH 03055, USA

S. VALTIERRA
Research and Development, Corporativo Nemak, S.A. de C.V., P.O. Box 100 Bosques del Valle, Garza Garcia, N.L. 66221, Mexico

The present study was carried out to determine the effect of alloy composition and solidification conditions on changes in the dendritic and eutectic structures in Al–Si alloys containing strontium. A series of experimental and industrial alloys viz., Al-7% Si, Al-12% Si, 319 and 356 were selected, to cover a variety of alloy freezing ranges. The techniques of thermal analysis, optical microscopy, and SEM/EDX and EPMA analyses were employed to obtain the results presented here. Depression in the eutectic Si temperature in Al-7% Si alloys occurs on addition of alloying elements such as Mg and Cu. Introduction of Sr to these alloys further depresses the eutectic temperature, with a corresponding increase in the volume fraction of the α-Al phase. The primary dendrite solidification pattern changes from parallel rows to a branched form, producing an equiaxed type of structure and hence shorter primary dendrite lengths. This is expected to enhance the interdendritic feedability. The lengths of the secondary dendrite arms are controlled by the rejection of solute atoms in front of the growing dendrites during solidification. The higher the alloying content in the alloy (i.e., 319), the smaller the dendrite cell size. The longer solidification time in the 319 alloy also appears to have a considerable influence on the amount of porosity formed in the alloy, in addition to that of Sr.

1. Introduction

The strength and quality of an Al—Si alloy casting are determined by the quality of its microstructure, viz., the fineness of the structure, the shapes and morphologies of the microconstituents present therein, as well as the amount of porosity produced in the casting. Normally, the microstructure is controlled through the processes of grain refinement and modification, using small additions of Al—Ti—B and Al—Sr master alloys, respectively. Whereas grain refinement primarily reduces the grain size, modification—using elements such as Na, Sr, Sb, or even rare earths—alters the morphology of the eutectic Si from its usual acicular brittle form to a fibrous form (in the case of Na and Sr) that is extremely beneficial to the mechanical properties, particularly the ductility. Among the various modifiers in use, strontium has, by far, been employed most extensively. Although easier to handle than either Na or the toxic Sb, and more resistant to fade (i.e., losing its modifying effect after a certain amount of time), Sr addition is also associated with porosity formation in these alloys.

From the feedability-related point of view, it has been pointed out that one should look to the Al—Si eutectic region of solidification to account for the differences in porosity observed when Sr is added to Al—Si melts [1–3]. Given that the eutectic constitutes a sizeable fraction of the microstructure of Al—Si alloys (depending on the Si level), it would be expected that the Sr-modified eutectic structure would exert some sort of influence on porosity formation. In this connection, Dahle *et al.* [4], who observed an orientation relationship between the α-Al dendrites and eutectic Si in unmodified hypoeutectic Al—Si alloys, and a lack of it in the (200 ppm) Sr-modified alloys (using electron microdiffraction techniques), have suggested that this represents a change in the mode of eutectic nucleation—from that occurring near the α-Al dendrites in the Sr-free alloy, to that taking place within the eutectic liquid itself in the Sr-containing alloy. The mode in operation controls the distribution of the remaining liquid in the last stages of solidification when feeding becomes extremely difficult. This distribution, in turn, will define

the connectivity of the feeding channels, and thus determine the resultant porosity profile in the solidified casting.

It is the aim of the present study to show the changes in both α-Al dendritic and eutectic regions in Sr-containing Al–Si alloys. A series of experimental and industrial Al–Si casting alloys were selected for study, from simple experimental "binary" alloys such as Al-7% Si and Al-12% Si, to industrial 319 and 356 alloys, to cover a variety of alloy freezing ranges. It should be mentioned at the outset, that the "binary" alloys in the present study are termed "binary" only in the sense that Al and Si are their main constituents, as against other alloying elements that are present in addition in the 356 and 319 alloys.

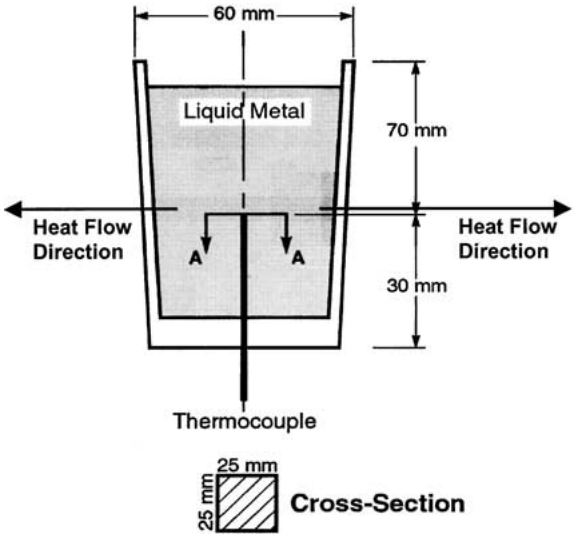

Figure 1 Schematic diagram of graphite mold used for thermal analysis and casting.

2. Experimental

Table I lists the chemical compositions of the various alloys that were used in the present work and their respective alloy codes. The alloys were cut into smaller pieces, cleaned, dried and melted in a 40 kg-capacity SiC crucible. The melting temperature was kept at 725° ± 5°C. The melts were degassed with dry argon for ~30 min, using a graphite rotary impeller (200 rpm; humidity of surroundings <15%). A 5 cm wide, 25 cm long plate made of refractory material, placed inside the crucible at an angle of ~35 degrees with the crucible wall, acted as a baffle during the melting and degassing process, to avoid vortex formation. In those cases when the melts were modified with Sr, the required amount of Sr was added to the melt using Al-10% Sr master alloy, before the degassing was carried out. All melts (experimental as well as industrial) were grain refined using Al-5%Ti-1%B master alloy (maximum attainable B was ~40 ppm). Samplings for chemical analysis were also taken simultaneously for each melt composition.

In the case of the experimental alloys, the alloys were first prepared by melting aluminum (purity 99.5%) at the same temperature, then adding pure silicon in the required amounts by means of a perforated graphite bell, to obtain the Al-7% Si and Al-12% Si alloys. The alloy melts were poured into ingot molds (made of mild steel and coated with refractory material). The solidified ingots in each case were then remelted for treatment as described above.

For each alloy melt composition, about 1 kg of the degassed melt was transferred by means of a ladle into a 1 kg-capacity SiC crucible (length/diameter ratio: 130 cm:85 cm) that was preheated at 750°C in a small electric resistance furnace. The transfer procedure was carried out with extreme caution to minimize turbulence, and took about 10 min. During the transfer, the SiC crucible was initially tilted at ~35 degrees, and then raised slowly while the liquid metal was poured into it, until it was in an upright position at the end of the filling. When the melt temperature in the crucible stabilized at 725°C, the melt was poured into a preheated (600°C) cyclindrical graphite mold (10 cm length, 6 cm diameter), as shown in Fig. 1. Again, for each pouring (into the graphite mold), a sampling for chemical analysis was also done simultaneously (the spectrometric analyses were carried out at GMPT, New Hampshire facilities).

Thermal analysis was carried out at the same time, by positioning a high sensitivity chromel-alumel (type K) thermocouple within the graphite mold system (through the bottom of the mold, halfway up into the mold cavity along the mold centerline, see Fig. 1). The temperature-time data was obtained using a high-speed data acquisition system (rate of 0.2 s) linked to a computer. From the thermal analysis data, cooling curves and their first derivatives were plotted. From these, the different reaction temperatures and solidification times were determined.

TABLE I Chemical compositions (wt%) of alloys used

Alloy	Code	Si	Fe	Cu	Mg	Mn	Cr	Ti	Sr	Al
Experimental										
Al-7% Si	A7S	6.74	0.1599	0.2825	0.0228	0.0316	0.0051	0.0246	0.0018	92.7
Al-7% Si + Sr	A7SS	6.71	0.1891	0.3656	0.0340	0.0331	0.0064	0.0274	0.0114	92.6
Al-12% Si	A12S	11.76	0.1451	0.1144	0.0119	0.0072	0.0012	0.0413	0.0010	87.9
Al-12% Si + Sr	A12SS	11.76	0.1451	0.1144	0.0119	0.0072	0.0012	0.0413	0.0245	87.8
Industrial										
319	A7SC	6.24	0.1084	3.683	0.0496	<0.0005	<0.0005	0.1332	0.0001	89.7
319 + Sr	A7SCS	5.81	0.1145	3.584	0.0552	<0.0005	<0.0005	0.1466	0.0115	90.2
356	A7SM	6.50	0.1211	0.0470	0.3194	0.0008	0.0008	0.1110	0.0001	92.8
356 + Sr	A7SMS	6.47	0.1332	0.0398	0.3283	0.0020	0.0020	0.1164	0.0070	92.8

For metallographic examination, samples (25 mm × 25 mm) were sectioned from the graphite mold castings (transverse section from the central part containing the thermocouple tip), mounted and polished. As can be seen from Fig. 1, the direction of heat flow is parallel to the section from which the samples were cut. The microstructures were analyzed using a Leco 2001 image analyzer in conjunction with an Olympus optical microscope. The eutectic Si particle characteristics (length, area, aspect ratio and density), volume fractions of the α-Al dendrites and eutectic Si particles, as well as the dendrite arm spacing (DAS) and lengths of primary and secondary dendrites were measured. For measuring the α-Al volume fractions, the samples were etched in Keller's reagent for the requisite amount of time, before the measurements were carried out.

3. Results and discussion

From the cooling curves obtained for each of the alloys listed in Table I, the corresponding Al–Si eutectic solidification temperatures (T_{eut}) were determined. A schematic diagram (Fig. A1) is provided in the Appendix to clarify the terminology pertaining to the parameters used in this section. The mushy zone-, eutectic-, and total solidification times were also determined. These are summarized in Table II. As expected, addition of Sr lowers the Al–Si eutectic solidification temperature in each alloy.

In the binary alloys, the total solidification time is roughly the sum of the mushy zone- and eutectic solidification times, where for the eutectic A12S alloy, the total solidification time equals its eutectic solidification time. In the 356 and 319 alloys, however, the total solidification times are much longer than the sums of the other two.

Comparing the Sr-free and Sr-modified conditions for the two alloys, the mushy zone times increase in the modified alloys, whereas the eutectic solidification times are almost the same in either condition (this will be discussed in more detail later on, with reference to Table V and Fig. 7). Also, compared to 356 alloy, the T_{eut} is some eight degrees lower in the 319 alloy (see Table II). This factor, together with the larger number of reactions occurring in the 319 alloy, result in its exhibiting a longer total solidification time than the 356 alloy.

TABLE II Cooling curve data

Alloy	Alloy code	T_{eut} (°C)	Solidification times (s)		
			Mushy zone	Al–Si eutectic	Total
Al-7% Si	A7S	573.0	150	195	351
Al-7% Si + Sr	A7SS	565.0	189	172	360
Al-12% Si	A12S	573.6	–	411	411
Al-12% Si + Sr	A12SS	566.7	34	365	399
356	A7SM	570.1	159	156	461
356 + Sr	A7SMS	563.8	194	154	479
319	A7SC	563.7	169	130	517
319 + Sr	A7SCS	555.8	195	129	529

TABLE III Temperatures and phases corresponding to peaks in Fig. 2

Figure	Peak	Temperature (°C)	Phases/Reactions
2(a) A7S alloy	A	608.8	Formation of α-Al dendritic network
	B	559.5–561	Eutectic Si
	C	553.6	Co-eutectic Al_2Si_2Sr
	D	537.9	Post-eutectic Al_2Si_2Sr
2(b) A7SCS alloy	A	611	Formation of α-Al dendritic network
	B	555.8	Eutectic Si
	C	540.6–533.2	α- & β-Fe phases, Al_2Si_2Sr
	D	516.1	$CuAl_2$
	E	508.5	$Al_5Mg_8Si_6Cu_2$

Fig. 2 displays the cooling curves and first derivatives for Sr-modified Al-7% Si and 319 alloys. The peaks marked A through E are listed in Table III, and were identified with reference to the atlas of Backerud *et al.* [5] on the solidification of aluminum foundry alloys. In the case of the A7SS (modified Al-7% Si) alloy, the three main reactions observed correspond to the formation of the α-Al dendrite network (peak A), followed by precipitation of the Al–Si eutectic (peak B), and, due to the presence of Sr (in amounts higher than that required for obtaining a fully modified eutectic structure), the co-eutectic and post-eutectic precipitation of Al_2Si_2Sr phase (marked C and D in Fig. 2a). In the A7SCS (modified 319) alloy, Fig. 2b, several additional reactions occur, corresponding to the precipitation of the α- and β-Fe intermetallics (peak C, over a range of temperature), and the precipitation of the copper intermetallics (peaks D and E). Noticeable differences in the end-of-solidification times and temperatures between the two alloys are also observed (see Table II for actual values).

The significance of the longer total solidification time exhibited by the 319 alloy (cf. A7S alloy, Table II) may be judged from a comparison of the percentage porosity levels observed in the corresponding metallographic samples of these two alloys, obtained from their graphite mold/thermal analysis castings (DAS ~85 μm). As Table IV shows, the percentage porosity jumps from 0.36% in the Al-7% Si alloy to 2.2% in the 319 alloy, whereas a 250 ppm Sr addition to 319 hardly alters its porosity level. On the other hand, modifying the 'binary' alloy doubles its porosity content, i.e., alters it significantly. In other words, while the addition of Sr increases the porosity in binary Al–Si

TABLE IV Percentage porosity observed in Al-7% Si and 319 alloys

Alloy	Hydrogen level (mL/100 g)	Percentage porosity (%)			
		Alloy code[a]	No Sr	Alloy code[a]	250 ppm Sr
Al-7% Si	0.1	A7S (*351s*)	0.36	A7SS (*360s*)	0.86
319	0.1	A7SC (*517s*)	2.2	A7SCS (*529s*)	2.3
	0.25[b]		2.86[b]		3.4[b]

[a]Total solidification times (s) given in parentheses below the alloy codes.
[b]Gassed melt.

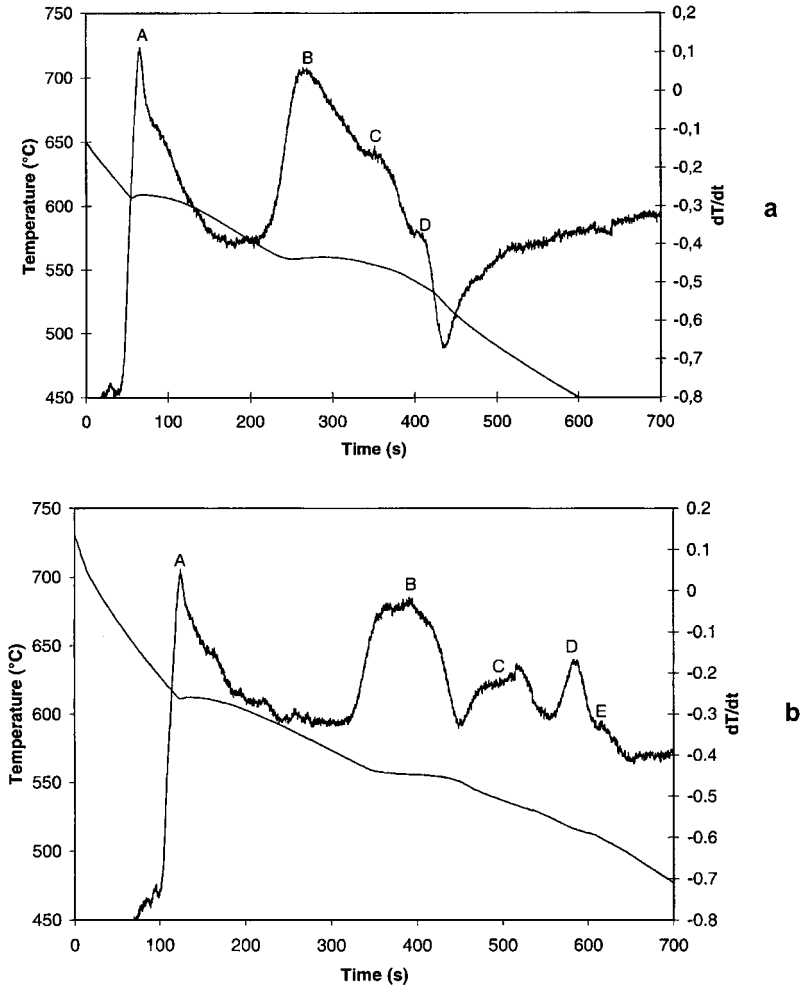

Figure 2 Cooling curves and first derivatives obtained for Sr-modified: (a) Al-7% Si and (b) 319 alloys.

alloys, the longer solidification time in the 319 alloy also appears to have a considerable influence on the amount of porosity formed in the alloy (viz., in alloys containing a higher number of alloying elements), in addition to that of Sr.

It could be argued that this does not establish the importance of solidification time *per se* in that other factors such as heat transfer rates have not been considered. However, given the fact that the graphite mold castings from which these samples were prepared were obtained under very similar experimental (i.e., melt- and mold temperature) conditions, it would not be unreasonable to consider it as an influential parameter.

As will be discussed later on in another context, Table IV also shows that, compared to the porosity values obtained from well-degassed 319 alloy melt samples (hydrogen level ~0.1 mL/100 g), the porosity levels displayed by samples taken from 319 alloy melts that were deliberately gassed (hydrogen content ~0.25 mL/100 g) were comparatively much higher.

The phenomenon of feedability has been looked at from two viewpoints: (a) the freezing range of the alloy, and (b) the effect of eutectic solidification, viz., the nature of the Al–Si eutectic solidification front. The difference between the liquidus and solidus temperatures of an alloy defines its equilibrium freezing range, and a short freezing range is considered best for interdendritic feeding. The permeability of the region between these two temperature points controls the feeding and, hence, the microporosity that is expected to result upon solidification.

Quenching experiments on samples of unmodified and modified Al–Si eutectic alloys [6, 7] appear to indicate that the solid/liquid interface is more or less smooth and regular (or planar) in modified Al–Si alloys, whereas it is highly irregular in the unmodified alloys. Consequently, it has been suggested that liquid entrapment and porosity formation would be more likely to occur during eutectic solidification in unmodified alloys than in the modified alloys.

Argo and Gruzleski [8] proposed a two-stage solidification process to account for microshrinkage formation in unmodified vs. modified alloy castings. According to them, a short interdendritic feeding distance in the unmodified alloy (represented by a smaller number of secondary dendrite arms per primary Al-dendrite) allows for easier feeding, so that microshrinkage formation takes place in the last region to solidify. The irregular solid/liquid interface then facilitates the distribution of microporosity in this region. A longer mushy zone (which reduces the feedability) in the case of the modified alloy results in a wider dispersion of isolated pockets of eutectic liquid, which then solidify with a regular solid/liquid interface, producing larger pores than those observed in the unmodified case.

In the present study, the microstructures of the four sets of unmodified-modified alloys (i.e., A12S-A12SS, A7S-A7SS, A7SM-A7SMS (356), and A7SC-A7SCS (319)) were examined to discern any differences in the development and growth of the α-Al dendrites and that of the Al–Si eutectic between the unmodified and modified alloys and to compare them with the observations reported in the literature.

Fig. 3 shows the microstructures obtained for the A12S and A12SS alloys. In both cases, the majority of the microstructure consists of the Al–Si eutectic, with a small amount of primary α-Al dendrites observed therein. The Si particles are acicular in the unmodified alloy, Fig. 3a, and very fine in the modified alloy, Fig. 3b. The pattern of the dendrites gives an indication of the growth of the dendrites along the direction of heat flow. In comparison to the lack of exaggerated growth in any particular lateral direction observed in Fig. 3a, in the modified alloy, Fig. 3b, due to the undercooling that occurs with the addition of Sr, the increased temperature difference between the liquidus and solidus (and thus a steeper thermal gradient) permits the growth of larger, branching dendrites whose lengths appear to be more prominent compared to their other dimensions. As the temperature falls monotonically from the hot interior liquid to the freezing interface and further on to the mold wall, the freezing front persists as a simple plane normal to the temperature gradient. The parallel rows of dendrites observed in Fig. 3b confirm this.

In the high magnification micrographs of the two alloys shown in Fig. 4, if one looks closely, it can be seen that the contours of the dendrites in the unmodified alloy, Fig. 4a, are, in fact, also regular. It is only the acicular nature of the Si particles in the one case (A12S), and their fineness in the other (A12SS), that accentuates the smoothness of the dendrite contours in the latter case, Fig. 4b.

Under quiescent or rapid cooling conditions, the melt just ahead of the freezing interface is always undercooled, so that it is actually at a lower temperature than the adjacent solid. This is because of the release of latent heat of fusion (into both the liquid and the solid). If some point in the freezing front advances ahead of the rest, it finds itself in liquid that can absorb heat and encourage further freezing. These random points grow into spikes and the freezing front loses its planar character. Due to the undercooling that occurs in the Sr-modified alloy, the regularity of the dendrites in Fig. 4b is marred by such spikes (see arrow, for example), resulting in the irregularly shaped dendrites observed in the figure.

Fig. 5 shows the microstructures of the A7S, A7SM (356), A7SS, A7SMS (356), and A7SCS (319) alloys, respectively. Compared to the unmodified alloys

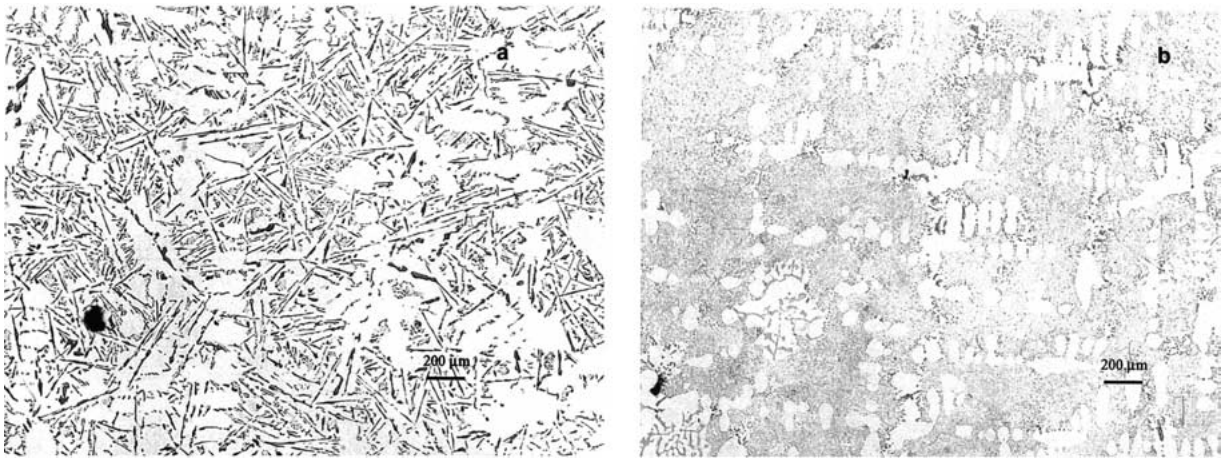

Figure 3 Optical micrographs showing the dendrite morphology in (a) unmodified and (b) Sr-modified Al-12% Si alloy.

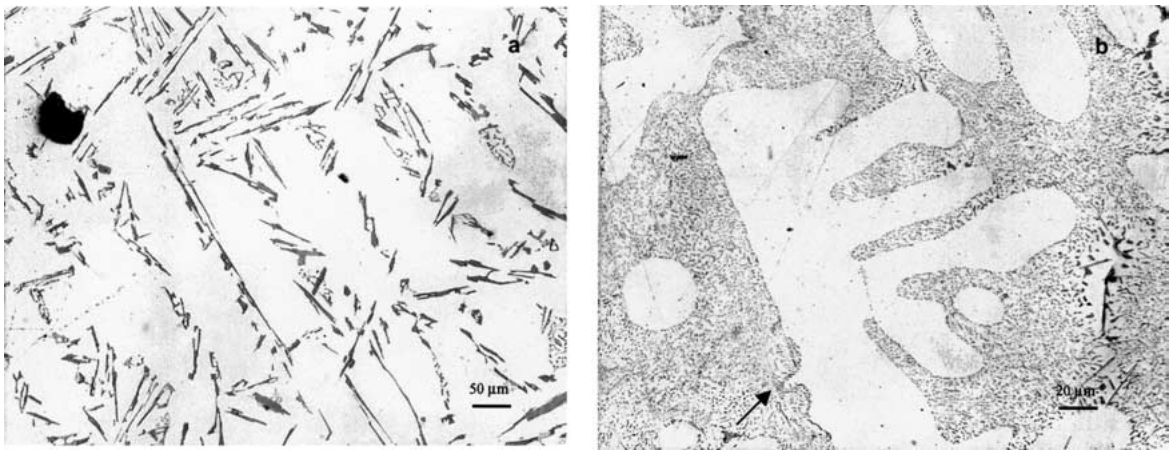

Figure 4 High magnification micrographs of Al-12% Si alloy showing: (a) uniform dendrites in the unmodified alloy and (b) comparatively irregular dendrites in the modified alloy (arrow indicates a dendrite nucleation site).

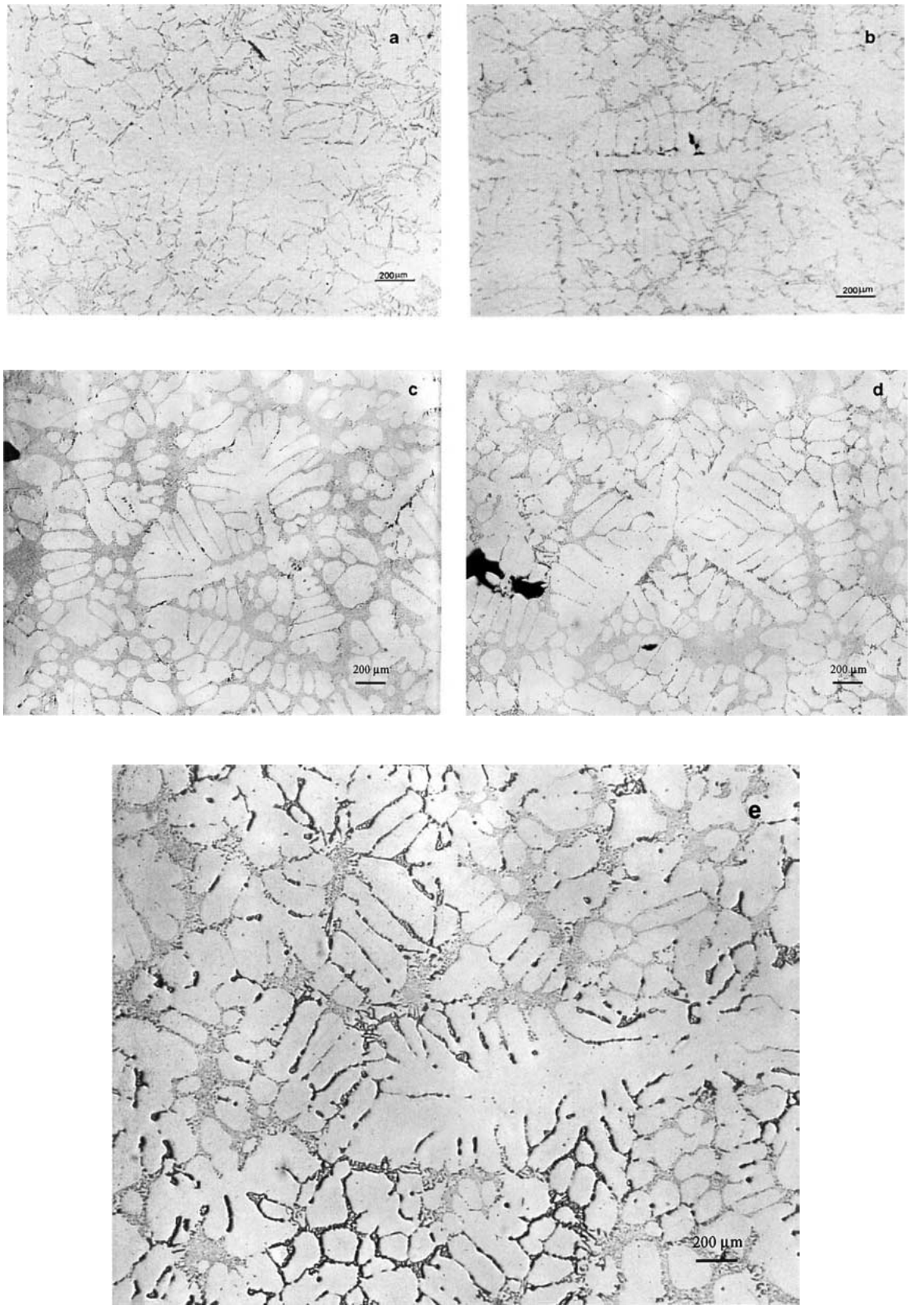

Figure 5 Optical micrographs showing the secondary dendrite formation in unmodified (a) Al-7% Si, (b) 356, and modified (c) Al-7% Si, (d) 356, (e) 319 alloys, where the mollified alloys show a more equiaxed dendrite structure.

(Fig. 5a and b), the modified alloys (Fig. 5c, d and e) show a more equiaxed dendrite structure. In the case of the modified 319 alloy, Fig. 5e, the interdendritic regions are filled with the copper phase ($CuAl_2$), as delineated by the darkened contours of the α-Al dendrites (cf. the fine, light grey dotted Al–Si eutectic areas appearing in other interdendritic regions in the micrograph). Although the copper phase particles are not clearly observed in Fig. 5e, they were confirmed to be the $CuAl_2$ phase occurring either as the Al-$CuAl_2$ eutectic or in its block-like form [9], when observed at high magnification (200×).

Yang *et al.* [10] have proposed a model for the simulation of microstructural evolution in multicomponent Al–Si alloys (viz., 356 alloy) with equiaxed dendritic and eutectic morphology, based upon the mixture-theory (continuum approach) model. In general, the growth velocity of equiaxed dendrites and eutectic can be calculated as a function of the undercooling ΔT as

$$dr_E/dt = \mu \cdot (\Delta T)^2 \quad (1)$$

where r_E is the radius of the eutectic grain or of the *equivalent dendrite envelope*, and μ is a growth coefficient which depends on the type of equiaxed grain. The growth coefficient is different for primary phase and eutectic grains. The *dendrite envelope* is defined as the surface touching the tips of all primary and secondary arms, and the *equivalent dendrite envelope* is the sphere having the same volume as the dendrite envelope. The driving force for the dendrite growth is determined by the melt undercooling at the tip of the primary dendrite (grain). In binary alloys, for dendrite growth, constitutional and thermal undercooling are the controlling factors, while in the case of eutectic growth, thermal undercooling is assumed to be the controlling parameter.

The four solidification parameters of interest are the liquidus temperature (T_L), the eutectic temperature (T_E), the liquidus slope (m_L) and the partition coefficient (k), and can be calculated easily from the phase diagrams of binary alloy systems. When considering multicomponent alloys (such as 356 or 319), however, the solute transport equations must be solved for each component element, i.e., the slopes and partition coefficients must be known for each in order to determine their effect on the equilibrium temperatures.

Such complicated theoretical calculations are not within the scope of the present experimental study. Nevertheless, on the basis of the temperature and time data gathered from the cooling curves, and the microstructural observations and image analysis measurements, certain fundamental conclusions can still be made. From Equation 1, the more the undercooling, the faster will be the growth rate of the dendrites, as is the case for the modified alloys. This would account for the equiaxed dendrite structures observed in Fig. 5c through e.

Image analysis measurements were also carried out on these alloy samples, where the α-Al dendrite and eutectic Si particle characteristics and volume fractions were measured. The measurements were carried out over a certain number of fields ("field" denoting the field of observation of the optical microscope, and covering an area of 1.41301×10^5 μm^2 at 200× magnification), such that the entire sample surface was traversed in a regular, systematic fashion. From these, the average α-Al and average eutectic Si volume fractions were determined. The corresponding values and their standard deviations (SD) are plotted in Fig. 6.

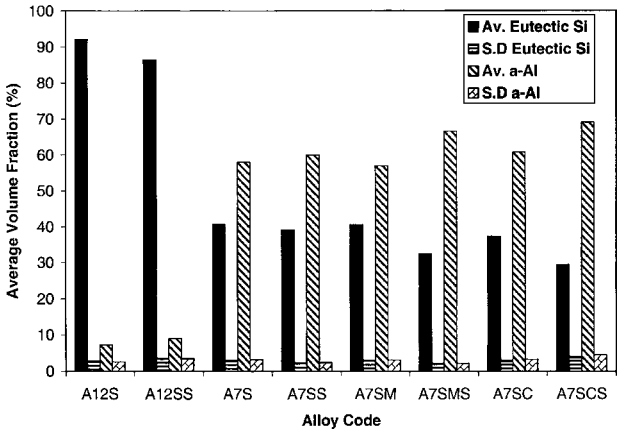

Figure 6 Volume fractions of α-Al and eutectic Si in the four alloy types studied.

From Fig. 6, it is seen that, regardless of the alloy composition, the addition of Sr increases the α-Al volume fraction, with a corresponding decrease in the amount of eutectic Si. Comparing the three 7% Si-containing alloys (viz., A7S, A7SM and A7SC), both the increase in the amount of alloying elements in the alloy and the addition of Sr will affect the decrease in the eutectic solidification temperature so that the amount of α-Al phase will increase on passing from A7S to A7SM (356) to A7SC (319) alloys (in either unmodified or modified alloys). The enlarged sections of the cooling curves in Fig. 7 compare the amount of undercooling observed in the 356 and 319 alloys in both unmodified and modified conditions.

Primary dendrites for which a good number of secondary dendrites could be clearly observed were also measured for each structure. Table V lists the longest primary dendrite lengths that were observed in each case, and the corresponding number of secondary dendrites associated with each primary dendrite. From these values, the average thickness of the secondary dendrites could be calculated. The lengths of some 20–25 secondary dendrite arms were also measured from each alloy sample, to determine their average lengths. These are also listed in Table V. From columns 3 and 4 of the table, it can be seen clearly that in the case of the

TABLE V Primary and secondary α-Al dendrite measurements

Alloy	Alloy code	Max. primary dendrite length (μm)	No. of secondary dendrite arms	Av. thickness of secondary dendrite arms (μm)	Av. length of secondary dendrite arms (μm)
Al-7% Si	A7S	664	10	66.4	153.4
Al-7% Si + Sr	A7SS	1019	15	67.9	196.6
Al-12% Si	A12S	699	16	43.7	26.2
Al-12% Si + Sr	A12SS	1421	31	45.8	56.6
356	A7SM	1155	17	67.9	189.7
356 + Sr	A7SMS	754	10	75.4	159.0
319	A7SC	790	15	52.7	133.1
319 + Sr	A7SCS	866	14	61.9	133.8

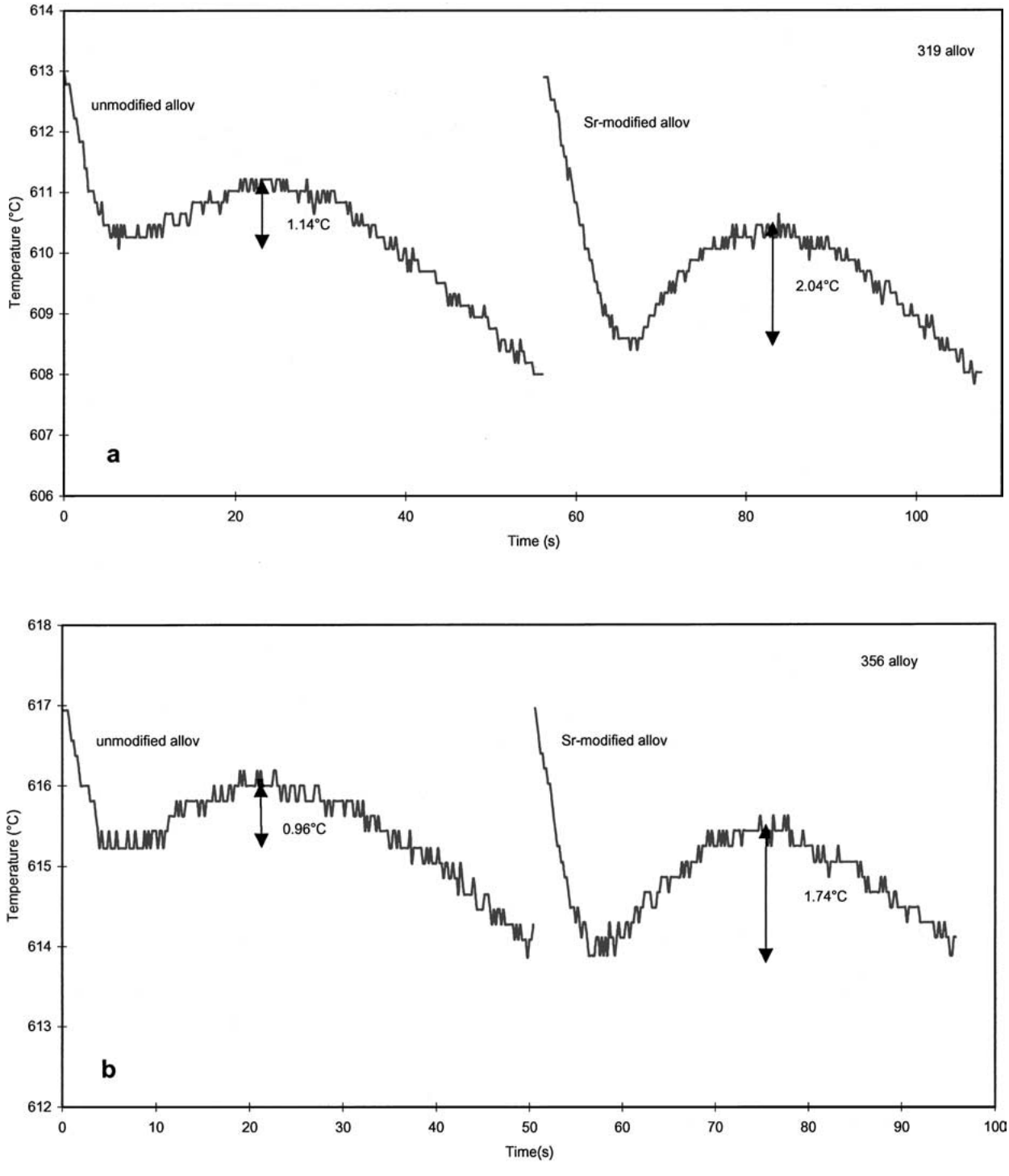

Figure 7 Enlarged sections of the cooling curves obtained for (a) 319 and (b) 356 alloys, comparing the undercooling observed in the unmodified and Sr-modified cases.

Al-7% Si and Al-12% Si alloys, the primary dendrite lengths increase with the addition of Sr, as do the number of secondary dendrite arms per primary dendrite, and the secondary dendrite arm lengths as well. These observations more or less conform to those of Argo and Gruzleski [8]. In the case of the 356 alloy, it is seen that the primary dendrite length decreases in the modified alloy, in keeping with the equiaxed dendrite structure observed in Fig. 5b. The increase in thickness of the secondary dendrite arms is partly due to the increase in the α-Al volume fraction, as well as their lateral expansion, as inferred from the reduction in the average length.

From the data presented thus far, we have seen (a) how the primary dendrites in the modified 356 alloy possess an equiaxed structure and, thus, shorter lengths, and (b) how the increase in the mushy zone period (α-Al precipitation) and, hence, α-Al volume fraction, reduces the interdendritic eutectic region (i.e., the Si volume fraction, Fig. 6). It has also been reported that Sr improves fluidity by 15–30% (Hu and Pan [11]; Samuel *et al.* [12]). Apparently, in view of these observations, Sr addition should improve the feedability of the interdendritic regions (and hence decrease the porosity). Thus, some other factor should be sought to account for the increase in porosity with the addition of Sr.

The 319 alloy shows practically no change in the number of secondary dendrite arms (per primary dendrite) or their average length between the unmodified and modified conditions. With a greater number of alloying elements present in the alloy, there is competitive growth between the dendrites and the eutectic (and other phases), due to the rejection of a considerable amount of solute in front of them with the progress of solidification. According to Yang *et al.* [10], both temperature and concentration must be considered for the start of the eutectic reaction in a multicomponent alloy such as 356 (which solidifies under non-equilibrium conditions), as the liquid concentration does not necessarily reach the eutectic concentration even if the temperature drops below the eutectic temperature. Thus, at any point in the casting, the eutectic reaction will start only if the two conditions

$$T_b < T_E \quad \text{and} \quad C_L^* \geq C_E$$

are satisfied, where T_b is the bulk temperature, T_E is the equilibrium temperature, C_L^* is the liquid concentration at the solid/liquid interface, and C_E is the initial composition of the eutectic reaction. Applying similar considerations to the 319 alloys, it is easy to understand why the dendrites in the 319 alloy appear as they do in Fig. 5e, and also why the secondary dendrite arm lengths do not change from the unmodified to the modified alloy (Table V).

In their study of the effect of phosphorus on the solidified structure of hypoeutectic Al-10% Si alloys (solidification rate 0.1 K/s), Kato *et al.* [13] have also reported that, with the addition of 50 ppm phosphorus, the α-Al dendrite growth is blocked due to the rejection of phosphorus. Likewise, the lengths of the α-Al dendrites are also decreased, similarly.

4. Conclusions

Based on the present work, the following two main conclusions could be drawn.

1. Depression in the eutectic Si solidification temperature in Al-7% Si alloys is caused by the addition of alloying elements such as Mg and Cu. Introduction of Sr to these alloys further depresses this temperature, with a corresponding increase in the volume fraction of the α-Al phase. The primary dendrite solidification pattern changes from parallel rows to a branched form, producing an equiaxed type of structure and hence shorter primary dendrite lengths. This is expected to enhance the interdendritic feedability.

2. The lengths of the secondary dendrite arms are controlled by the rejection of solute atoms in front of the growing dendrites during solidification. The higher the alloying content of the alloy (i.e., 319), the smal ler the dendrite cell size. The longer solidification time in the 319 alloy also appears to have a considerable influence on the amount of porosity formed in the alloy, in addition to the effect of Sr.

Acknowledgements

Financial and in-kind support received from the Natural Sciences and Engineering Research Council of Canada (NSERC), the Centre québecois de recherche et de développement de l'aluminium (CQRDA), the Fondation de l'Université du Québec à Chicoutimi (FUQAC), General Motors Powertrain Group (U.S.A), Corporativo Nemak (Mexico) and ABB Bomem Inc. (Quebec) is gratefully acknowledged.

Appendix

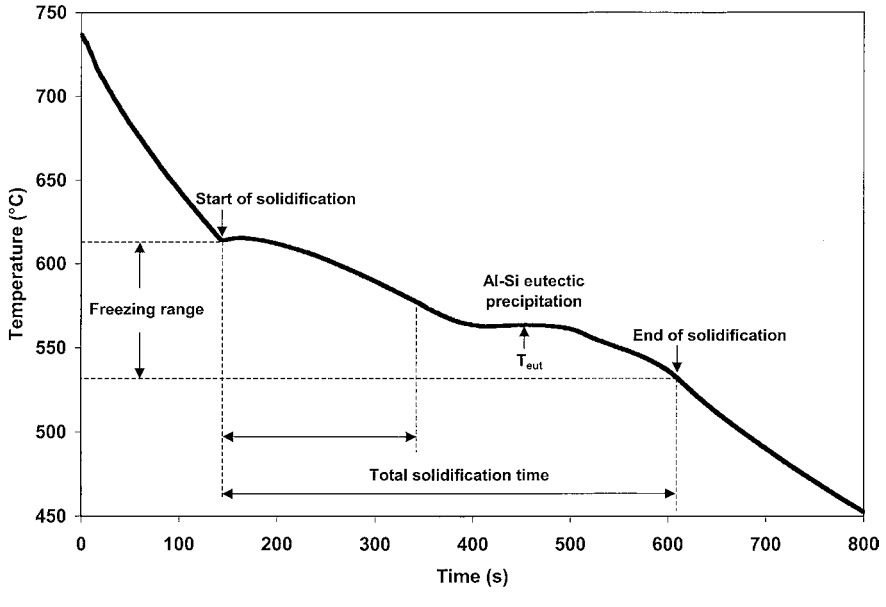

Figure A1 Schematic diagram of cooling curve of an Al–Si alloy defining the various solidification parameters (temperature and time) used in Section 3.

References

1. J. R. DENTON and J. A. SPITTLE, *Mater. Sci. Techn.* **1** (1985) 305.
2. G. K. SIGWORTH, *AFS Trans.* **91** (1983) 7.
3. J. M. KIM, H. W. KWON and C. R. LOPER Jr., *AFS Trans.* **104** (1996) 743.
4. A. K. DAHLE, J. HJELEN and L. ARNBERG, in Proc. 4th Decennal Int. Conf. on "Solidification Processing 1997" (University of Sheffield, Sheffield, UK, 1997) p. 527.
5. L. BACKERUD, G. CHAI and J. TAMMINEN, Solidification Characteristics of Aluminium Alloys, Volume 2: Foundry Alloys (AFS/Skanaluminium, Des Plaines, IL, 1990) pp. 71; 85; 135.
6. H. FREDRIKSSON, M. HILLERT and N. LANGE, *J. Inst. Metals* **101** (1973) 285.
7. S. C. FLOOD and J. D. HUNT, *Metal Science* **16** (1981) 287.
8. D. ARGO and J. E. GRUZLESKI, *AFS Trans.* **96** (1988) 65.
9. A. M. SAMUEL, J. GAUTHIER and F. H. SAMUEL, *Metall. Mater. Trans.* A **27A** (1996) 1785.
10. B. J. YANG, D. M. STEFANESCU and J. LEON-TORRES, *ibid.* A **32A** (2001) 3065.
11. J. F. HU and E. N. PAN, *Chukung, J. Chinese Foundrymen's Association* **23(1)** (1997) 48.
12. A. M. SAMUEL, F. H. SAMUEL, C. VILLENEUVE, H. W. DOTY and S. VALTIERRA, *Int. J. Cast Metals Res.* **14** (2001) 97.
13. E. KATO, H. NOMURA and N. OSHIRO, *J. Jpn. Instit. Light Metals* **47**(12) (1997) 667.

Received 8 November 2002
and accepted 18 August 2003